

Numerical Simulation of a Gas Turbine Combustor Using Nanosecond Pulsed Actuators

Chin-Cheng Wang*

Yuan Ze University, Chung-Li, Taoyuan 32003, Taiwan

and

Subrata Roy[§]

University of Florida, Gainesville, FL 32611-6300

We numerically predict nanosecond pulsed dielectric barrier discharge (DBD) actuators for combustion stabilization. Three problems are considered in the present study. First problem is a benchmark case which is compared with reported experimental data. Numerical results show good agreement with velocity components in axial-, radial- and tangential- directions. For the comparison of flame temperature, we also show similar trend with the experiment. For the second problem, we employ serpentine plasma actuator for plasma assisted combustion. We numerically investigated the influence of inner and outer recirculation zones interacts with the serpentine plasma actuators. Also, the details of the flame shape and combustion stabilization mechanism are examined. The last problem is to use nanosecond pulsed plasma actuators for stabilizing the flame. The results show that the nanosecond pulsed actuators are able to stabilize the flame near the walls. This may also enhance combustion efficiency for a lean-burn condition.

Nomenclature

$D_{e,m,p}$	=	electron, negative ion or positive ion diffusion coefficient (m ² /s)
E	=	electric field (V/m)
e	=	elementary charge (C)
F_E	=	electric force density (N/m ³)
J	=	current density (A/m ²)
k_B	=	Boltzmann's constant (J/K)
k_e	=	turbulent kinetic energy (m ² /s ²)
$n_{e,m,p}$	=	electron, negative ion or positive ion density (m ⁻³)
P_{Th}	=	power deposition (W/m ³)
p	=	pressure (Torr)
q	=	charge density, $(n_p - n_m - n_e)$ (m ⁻³)
$r_{ep,np}$	=	electron-ion or ion-ion recombination rate (m ³ /s)
$T_{e,m,p}$	=	electron, negative ion or positive ion temperature (K)
t	=	time (s)
V_B	=	Bohm velocity (m/s)
$V_{e,m,p}$	=	electron, negative ion or positive ion velocity (m/s)
V	=	fluid velocity (m/s)
α	=	ionization coefficient (m ⁻¹)
ε	=	dielectric constant (Farad/m)
ϕ	=	potential (V)
Γ_e	=	electron flux (m ⁻² s ⁻¹)
η	=	attachment coefficient (m ⁻¹)
λ	=	thermal conductivity (W/mK)
$\mu_{e,m,p}$	=	electron, negative ion or positive ion mobility (m ² /sV)
μ_t	=	turbulent dynamic viscosity (kg/sm)

* Assistant Professor, Department of Mechanical Engineering, Member AIAA, ccwang@saturn.yzu.edu.tw

§ Associate Professor, Department of Mechanical and Aerospace Engineering, Associate Fellow AIAA, roy@ufl.edu

μ	=	fluid viscosity (kg/sm)
ρ	=	fluid density (kg/m ³)
τ	=	viscous stress tensor (N/m ²)
$\dot{\omega}_k$	=	reaction rate of species (kg/sm ³)
$\dot{\omega}_T$	=	heat release (W/m ³)

I. Introduction

In 2011, over 82 percent of the energy used in the United States was produced by combustion sources [1]. Combustion is still the key energy in our daily life. However, combustion also affects climate change through emissions such as unburned or partially burned hydrocarbons, nitrogen oxides, carbon monoxide, sulfur oxides, particles, and greenhouse gases. Some of pollutants are able to avoid, but some of them are very hard to reduce especially carbon dioxide. If we can increase the fuel efficiency, these emissions may also be reduced. Our objective is to enhance the performance of combustion by using nanosecond pulsed plasma actuators for a gas turbine combustor.

Moreau [2] and Corke *et al.* [3] showed detailed reviews of aerodynamic applications of plasma dielectric barrier discharge (DBD) actuators are effective in controlling the flow. The plasma actuators produce a significant thrust by asymmetric spanwise electrode configurations through momentum transfer. The momentum transfer between the plasma and gas happens due to collisional momentum transfer between charged ions and neutral atoms. Such actuation of the flow is active and near instantaneous. The advantages of the plasma actuators are without moving parts and easy to compact on any location. Compared to conventional actuators for active flow control, the life of DBD actuators will be much longer than mechanical reciprocal devices such as synthetic jet actuators.

Experiments and simulations have shown that the momentum boundary layer is significantly influenced by plasma actuation in low speed regime. Gaitonde and Visbal *et al.* [4-5] investigated control of three-dimensional vortical structures using plasma DBD actuators. In their studies, the three-dimensional vortical structures were analyzed using essentially two-dimensional plasma effects. They showed the wake region behind the airfoil has been reduced. However, nonequilibrium plasma DBD actuators find limited application for high speed flows. This is due to inherent losses associated with the momentum exchange between the charged and neutral particles, and due to exorbitant power budget. As an alternative, high-voltage nanosecond pulsed plasma actuators are becoming quite attractive option for high speed application [6].

The main mechanism of impact for nanosecond pulsed plasma actuators is the energy transfer. Recently experimental results [7] reported that nanosecond pulsed voltage is highly efficient to control boundary layer separation, lift and drag force coefficients, in addition to acoustic noise reduction in the Mach number range 0.05–0.85. Their measurements showed the mean temperature of 400 K for 50 ns pulse durations. Such fast heating (less than microsecond) of the gas layer leads to periodic flow disturbances that control boundary layer separation and reduce acoustic noise at the Mach number close to one.

Recently, studies of plasma assisted combustion (PAC) have shown many possibilities for improving combustion efficiency. A detailed review provided by Starikovskiy and Aleksandrov [8] shows the potential use of nonequilibrium plasma for ignition and combustion control has been an increasing interest in flame stabilization. Stage *et al.* [9] showed the effect of plasma on the flame. When the plasma is applied with increasing the plasma power, the flame propagation speed is also increased and towards the electrodes. They mentioned the combustion enhancement may result from the breakdown of fuel and the creation of reactive radicals. Leonov *et al.* [10] reported three concepts of PAC which are (i) the enhancement of chemical reactions due to heating and active particle generation, (ii) mixing oxidizer with fuel in flow and (iii) flow structure modification for combustion stabilization. These concepts of plasma discharges have been proved for ignition and combustion control [11]. They [10] also reported that there are at least four possible mechanisms of PAC which are (i) fast local ohmic heating of the medium, (ii) non-equilibrium excitation and dissociation of oxygen and fuel molecules, (iii) momentum transfer in electric and magnetic fields and (iv) shocks/instabilities generation. The main reason of using nanosecond pulsed plasma actuator is because it has combined effect of momentum and energy transfer from plasma to the neutral gas.

In our prior study [12-13], we presented the serpentine actuator induced flow mixing on a flat surface and a gas turbine combustor. The results showed three-dimensional plasma effects extract momentum from an upstream flow injecting it into the bulk fluid through localized pinching and spreading effects. Such three-dimensional novel actuators produce much better flow mixing downstream of the actuator than standard two-dimensional (linear) actuator. We showed the swirl generated by the serpentine actuators creates local low velocity regions stabilizing the flame. The purpose of present study is to introduce nanosecond pulsed actuator for flame stabilization. Roy *et al.* [14-16] presented a well-established first-principles plasma model to describe detailed densities of electrons, positive and negative charged and neutral species with Poisson's equation to obtain temporal and spatial profiles of voltage and densities. For accurate distribution of momentum and energy transfer, we employ physics based first-principles analysis to resolve the plasma force vectors and the distribution of power deposition over the surface. The detailed numerical model is summarized in section II. Section III describes the cases of numerical simulation. Section IV presents the results. Finally, conclusions are drawn in section V.

II. Numerical Model

A two-dimensional three-species hydrodynamic model is employed for multi-scale plasma discharge simulation at atmospheric pressure. The model uses an efficient finite element algorithm. The unsteady transport for positive ions, negative ions as well as electrons is derived from fluid dynamics in the form of mass and momentum conservation equations. The species momentum is modeled using the drift-diffusion approximation under isothermal condition that can be derived from the hydrodynamic equation. At atmospheric pressure, the drift-diffusion approximation is reasonable and computationally efficient. The continuity equations for positive ions, negative ions and electrons are given by:

$$\frac{\partial n_p}{\partial t} + \frac{\partial (n_p V_{pj})}{\partial x_j} = \alpha |\Gamma_e| - r_{ep} n_p n_e - r_{mp} n_p n_m \quad (1)$$

$$\frac{\partial n_m}{\partial t} + \frac{\partial (n_m V_{mj})}{\partial x_j} = \eta |\Gamma_e| - r_{mp} n_m n_p \quad (2)$$

$$\frac{\partial n_e}{\partial t} + \frac{\partial (n_e V_{ej})}{\partial x_j} = (\alpha - \eta) |\Gamma_e| - r_{ep} n_e n_{pe} \quad (3)$$

$$|\Gamma_e| = \sqrt{\sum_j (n_e V_{ej})^2}, \quad 1 \leq j \leq 2 \quad (4)$$

where $n_{p,m,e}$ are the number densities of the charged particle, subscript p , m , and e are positive ions, negative ions and electrons, respectively. $V_{p,m,e}$ are the species hydrodynamic velocities, α is the ionization coefficient, η is the attachment coefficient, $r_{ep,mp}$ are the electron-ion and ion-ion recombination coefficients, $|\Gamma_e|$ is the electronic flux and subscript j is the coordinate direction (i.e. $j = x, y$). The drift-diffusion form of ionic and electronic fluxes without external magnetic field in Eq. (1)-(3) are written as:

$$n_p V_p = n_p \mu_p \mathbf{E} - D_p \nabla n_p \quad (5)$$

$$n_m V_m = -n_m \mu_m \mathbf{E} - D_m \nabla n_m \quad (6)$$

$$n_e V_e = -n_e \mu_e \mathbf{E} - D_e \nabla n_e \quad (7)$$

where the electrostatic field is given by $\mathbf{E} = -\nabla \phi$, $\mu_{p,m,e}$ are the charged particle mobilities which are based on tabulated functions of the reduced electric field (E/N) [17], $D_{p,m,e} = \mu_{p,m,e} k_B T_{p,m,e} / e$ are the diffusion coefficients calculated from the Einstein relation which is a function of the mobility ($\mu_{p,m,e}$), Boltzmann's constant (k_B), the constant temperatures ($T_{p,m} = 300$ K, $T_e = 11600$ K), and the elementary charge ($e = 1.6022 \times 10^{-19}$ C). The ion and electron drift velocities depend mainly on the electric field. So all the transport coefficients are expressed as a function of a reduced electric field (E/N). The working gas is an air-like N_2/O_2 mixture. The mobilities, diffusion rates and rate coefficients for air-like mixture are obtained from the reference [17-19]. The relation between electric field (E) and charge separation (q) is given by the Poisson's equation:

$$\nabla \cdot (\epsilon \mathbf{E}) = e(n_p - n_m - n_e) = q \quad (8)$$

where ϵ is the permittivity. The coupled systems of species equations (1)-(3) as well as Poisson's equation (8) are solved using the in-house MIG flow code. The following boundary conditions are enforced. At the exposed electrode, the electronic flux is based on the electron thermal velocity and is directed towards the electrode. The

positive ion flux normal to the exposed electrode is considered as zero if the electric field is greater than zero. In the plasma domain of top, left and right boundaries, the homogeneous Neumann boundary condition is imposed (i.e. the slopes of the solution variables are equal to zero). The initial ion and electron number densities are assumed to be uniform and equal to 10^{15} m^{-3} in the plasma domain, while the charged particle densities are equal to zero in the dielectric material.

A commercial flow solver, ANSYS FLUENT, is used for combustion simulation. For unity Lewis number, a one-step global reaction mechanism is used for methane/air combustion. The single irreversible reaction equation is described as $\text{CH}_4 + 2(\text{O}_2 + 3.76\text{N}_2) \rightarrow \text{CO}_2 + 2\text{H}_2\text{O} + 7.52\text{N}_2$. The eddy-dissipation model that provides a turbulence chemistry interaction is chosen for calculating the single step heat release mechanism. The numerical model of reacting flows is governed by the Favre averaged conservation equations (9)-(12) for mass, momentum, chemical species, and enthalpy shown below [20]:

$$\frac{\partial \bar{\rho}}{\partial t} + \frac{\partial}{\partial x_j} (\bar{\rho} \tilde{V}_j) = 0 \quad (9)$$

$$\frac{\partial (\bar{\rho} \tilde{V}_i)}{\partial t} + \frac{\partial}{\partial x_j} (\bar{\rho} \tilde{V}_j \tilde{V}_i) = -\frac{\partial \bar{p}}{\partial x_i} + \frac{\partial}{\partial x_j} (\bar{\tau}_{ji} - \bar{\rho} \tilde{V}_j \tilde{V}_i^*) + \mathbf{F}_E \quad (10)$$

$$\frac{\partial (\bar{\rho} \tilde{Y}_k)}{\partial t} + \frac{\partial}{\partial x_j} (\bar{\rho} \tilde{V}_j \tilde{Y}_k) = \frac{\partial}{\partial x_j} (\bar{V}_{k,j} \bar{Y}_k - \bar{\rho} \tilde{V}_j \tilde{Y}_k^*) + \bar{\omega}_k, \quad k = 1, 5 \quad (11)$$

$$\frac{\partial (\bar{\rho} \tilde{h}_s)}{\partial t} + \frac{\partial}{\partial x_j} (\bar{\rho} \tilde{V}_j \tilde{h}_s) = \bar{\omega}_r + \frac{\overline{Dp}}{Dt} + \frac{\partial}{\partial x_j} (\lambda \frac{\partial T}{\partial x_j} - \bar{\rho} \tilde{V}_j \tilde{h}_s^*) + \tau_{ji} \frac{\partial V_j}{\partial x_i} - \frac{\partial}{\partial x_j} (\overline{\rho \sum_{k=1}^5 V_{k,j} Y_k h_{s,k}}) + \mathbf{P}_{Th} \quad (12)$$

$$\frac{\overline{Dp}}{Dt} = \frac{\partial \bar{p}}{\partial t} + \tilde{V}_j \frac{\partial \bar{p}}{\partial x_j} + \overline{V_j^* \frac{\partial p}{\partial x_j}} \quad (13)$$

where $\bar{\rho}$ is the average fluid density, \tilde{V} is the neutral gas mean velocity, V^* is the fluctuating velocity, \bar{p} is the average pressure, $\bar{\tau}$ is the average viscous stress tensor, \mathbf{F}_E is the electric force density, \tilde{Y} is the average species mass fraction, $\bar{\omega}_k$ is the average reaction rate of species, \tilde{h} is the average enthalpy, $\bar{\omega}_r$ is the average heat release due to combustion, λ is the thermal conductivity, and \mathbf{P}_{Th} is the power deposition. The effect of plasma assisted combustion is incorporated into the Favre average balance equations for momentum and enthalpy equations through the time-averaged source terms via user defined functions (UDF). For the momentum equations, the electric force density is described as $\mathbf{F}_E = \frac{1}{w} \left[\sum_{i=1}^w e(n_p - n_m - n_e) \mathbf{E} \right]$, and w is the number of time stations in a cycle used for time-averaging. The power deposition can be assumed as $\mathbf{P}_{Th} = \frac{1}{w} \left[\sum_i^w (\mathbf{J}_p - \mathbf{J}_m) \cdot \mathbf{E} - \zeta_{EX} \mathbf{J}_e \cdot \mathbf{E} \right]$, where \mathbf{J} is the current density and ζ_{EX} is the 28% of the electron energy deposited into excited states of the gas [21]. The turbulent Reynolds stresses are described using viscous stress tensor for Newtonian fluids:

$$\overline{\rho \tilde{V}_j \tilde{V}_i^*} = -\mu_t \left(\frac{\partial \tilde{V}_j}{\partial x_i} + \frac{\partial \tilde{V}_i}{\partial x_j} - \frac{2}{3} \delta_{ji} \frac{\partial \tilde{V}_k}{\partial x_k} \right) + \frac{2}{3} \bar{\rho} k \quad (14)$$

where μ_t is the turbulent dynamic viscosity, δ_{ji} is the Kronecker delta, and k is the turbulent kinetic energy. Here we choose two-equation $k-\varepsilon$ turbulent model to calculate the turbulent kinetic energy, k_e , and its dissipation rate, ε , in order to estimate the turbulent viscosity, μ_t .

III. Problem Description

We focus on the improvement of flame stabilization through plasma DBD actuators. Figure 1 shows schematic of a modified version of a gas turbine combustor from Weigand *et al.* [22]. There are two swirling air (central and annular) coming from the bottom wall of the center of the combustor. The incoming co-swirling oxidizer (N_2/O_2) is

supplied from a plenum through the annular ($D_i = 17$ mm; outer $D_o = 25$ mm) and central ($D = 15$ mm) nozzles. The non-swirling methane fuel (CH_4) is injected into the combustion chamber between two air nozzles. The combustion chamber had a square section of $85 \times 85 \text{ mm}^2$ and a height of 110 mm shown in Fig. 1. The chamber is connected by a top plate with a central exhaust tube of 40 mm in diameter. The actuators are installed at the side walls of $y = \pm 42.5$ mm and a height of $z = 10$ mm. Here, the electrodes are separated by a dielectric which can be the quartz plate in the experiment [22]. Appropriate designing of such plasma DBD actuators can help three-dimensional flow mixing [23]. The geometry of the serpentine actuator on the front and back walls is described in the inlay of Fig. 1. The width of the electrodes and the gap between electrodes were fixed at 2 mm. The plasma force vectors (thick purple arrows) are induced against the incoming air/fuel mixture for counter-flow electrode arrangement. In contrast, for the case of co-flow electrode arrangement, the actuators have been rotated 180 degrees along y -axis to actuate the incoming fresh air in the same axial (z) direction. In order to see the plasma effect through momentum transfer, we scale plasma force density by a factor of 100. Such plasma force may be obtained by using hundreds of watts. While rf powered serpentine plasma actuators may not be sufficiently strong for this augmentation, the local high-frequency nanosecond pulsed plasma actuators [6] will also be employed to enhance the performance of combustion.

We numerically test the system based on the parameters from “flame A” in Ref. [22]. We also compare our numerical solution of axial velocity on four different grids with experimental data at a height of $z = 5$ mm shown in Fig. 2. The largest error is located at the radial location of $y = 13$ mm where it is equal to 11.8 percent. In the present study, a structured mesh of 1.5 million nodes is used due to the less error of the axial velocity at a height of $z = 5$ mm. The cell size is ranged from 0.8 to 0.1 mm, which is sufficient to resolve the turbulence length scales. The mesh quality is maintained within the maximum aspect ratio of 10 and the skewness is less than 0.5. Figure 3 shows the computational grid and the location of the boundary conditions. At the bottom boundary, we employ velocity boundary conditions at a height of $z = 1.5$ mm from experiment data [22] for air and fuel flows instead of modeling of complicated swirl generators and a plenum. The air and fuel temperatures are set to 330 K. We impose no-slip boundary conditions on the adiabatic walls. For the outlet, a zero pressure condition is assumed at the top boundary. Three problems are investigated in the present study. The first problem is a benchmark case for verification. Our numerical results are compared with experimental data [22]. The second problem is to simulate the effect of serpentine plasma actuators on a gas combustor through momentum transfer. The last problem is to show the energy transfer inside a gas combustor via nanosecond pulsed plasma actuators. The results are described in the following section.

IV. Results and Discussion

For the benchmark case, figure 4 shows the comparison of experiment (left) and simulation (right) of time-averaged velocity vector plots at the central plane ($x = 0$) of the combustion chamber. Here, we can see very similar flow characteristics of the inner recirculation zone (IRZ) at the center and the outer recirculation zone (ORZ) near the walls on both experiment and simulation. The velocity vectors colored by black represent positive axial velocity, while the negative axial velocity vectors are displayed in red. For this type of confined swirl flame, IRZ ensures the mixing of the fuel with air, while ORZ mixes hot burned products into reactants near the flame base. Both experiment and simulation have almost the same jet angle of maximum mean velocity of 26 degree with respect to the axial centerline. Also, the center of recirculation regions are located at the similar heights for both IRZ and ORZ.

Figure 5 shows the comparison of experiment (dots) and simulation (solid lines) of time-averaged velocity components from the center ($y = 0$) to the wall ($y = 42.5$ mm) at $z = 5, 15$ and 45 mm. The numerical results of velocity components are in good agreement with previously reported experimental data [22]. At $z = 5$ mm, the positive maximum peak of 37 m/s and the negative minimum peak of -23 m/s in the axial velocity denote the inflow of the fresh gas and the inner recirculation zone, respectively. The simulated highest and lowest time-averaged axial velocities are close to the experimental peak values of 38 m/s and -21.5 m/s, respectively. The radial velocity is negative for the radial location of $y > 20$ mm representing the size of the ORZ. The maximum peak of the mean radial velocity in the IRZ is almost twice the size of that in the ORZ. For the tangential velocity, it seems rather flat (11.5 m/s) in the ORZ. In the IRZ, we can see two humps reflecting the swirling air from annular and central nozzles. The rather flat region between two humps is caused by the fuel injection. As the axial distance increases, the radial profiles of the radial and tangential velocity components become slightly flat shown in figure 5(b) and 5(c). Apparently, the axial velocity dominates the flow region at a height of $z = 45$ mm or above.

Figure 6 shows the comparison of experiment (dots) and simulation (solid lines) of time-averaged temperature at $z = 5, 10$ mm and the centerline ($y = 0$) as well as the two-dimensional contour. Our results numerically predict the temperature profile well from $y = 10$ mm to the walls at a height of $z = 5$ mm shown in Fig. 6(a). Although the predicted temperature is higher than the experimental data close to the centerline, we still compare well with other published numerical results [25]. This over prediction may result from a single step reaction mechanism. We can see much higher mean temperature occurs in the IRZ and ORZ than other regions. The lowest mean temperature of 400 K reflects the incoming fresh gas. As the height increases (at $z = 10$ mm) shown in Fig. 6(b), the lowest mean temperature rises and moves a little bit right due to the wider region of IRZ. Figure 6(c) shows the similar trend with experimental data except the centerline region. Figure 6(d) compares two-dimensional mean temperature profiles for experiment (left) and simulation (right). The simulated result shows much smoother changes in temperature than experimental data because we are solving Reynolds Averaged Navier Stokes (RANS) equations for a steady state solution.

For the second problem of serpentine plasma actuation, figure 7 plots the radial profiles of velocity components and velocity vectors for the cases of baseline (without plasma), co-flow serpentine actuation (with plasma), and counter-flow serpentine actuation (with plasma). At $z = 5$ mm shown in Fig. 7(a), the velocity components have substantial changes in the ORZ ($y = 20-40$ mm) for the counter-flow case denoting that the plasma actuation has a significant effect on the mixing of the fuel and air flows. At $z = 15$ mm, both cases of co-flow and counter-flow have considerable changes in the velocities near the walls because of the location of the plasma actuators (at $y = \pm 42.5$ mm; $z = 10$ mm). For the co-flow serpentine, the axial velocity in the IRZ is slightly lower than other cases indicating that more residence time is available. The size of IRZ and ORZ can also be observed from the radial velocity distribution in comparison to the baseline case. Specially, the counter-flow serpentine produces a strongest swirl (i.e. tangential velocity) in the IRZ, while the co-flow serpentine leads to the largest swirl in the ORZ. Figure 7(c) describes velocity vectors for the co-flow case (left) and counter-flow case (right) at the central plane ($x = 0$) of the combustion chamber. For the co-flow serpentine (left), it pinches and spreads fresh air in the vicinity of troughs and crests, respectively. Such plasma actuation (or disturbance) transfer momentum from ions to neutral gases to mix the surrounding fuel with oxidizer. In comparison to baseline case shown in figure 4, the size of the IRZ (at $y = \pm 30$ mm; $z = 70$ mm) of the co-flow case (left) is much bigger than the baseline case. Furthermore, the bigger IRZ means the wider low velocity region to stabilize the flame at the center. For the counter-flow case (right), a large ORZ are created near the walls to mix the cold incoming fresh air with hot burned gas. Apparently, the size of the ORZ from counter-flow case is wider than other two cases which are the baseline and the co-flow cases. However, the large ORZ from the walls may squeeze the size of the IRZ at the center. So the combustion may become unstable due to less residence time to anchor the flame at the base. Figure 8 shows the time-averaged temperature distribution for radial profiles at $z = 5$ mm, $z = 10$ mm and the centerline as well as two-dimensional contour. At $z = 5$ mm, all three cases exhibit similar trends which start from the highest temperature of ~ 1700 K then decrease to the lowest temperature of ~ 400 K and then rise to 1600 K. The low temperature region (at $y = 5-20$ mm) reflects the incoming cold swirl air, while the high temperature region is mainly due to the enhancement of flow mixing. At $z = 10$ mm, the serpentine plasma actuation shows a significant effect on the shapes of flame temperature. For the co-flow serpentine, the wider IRZ is able to increase the residence time for the mixing of fuel and oxidizer (i.e. cold fresh air). In contrast, for the counter-flow serpentine, the larger ORZ mixes hot products into reactants, and then increase the combustion temperature close to the walls. However, the increasing ORZ in the radial-direction from the walls may squeeze the size of IRZ near the center. Furthermore, if the IRZ becomes too small, it may cause combustion instability. For the centerline temperature seen in figure 8(c), here shows very similar trends for all three cases. The temperature should rise and reach a maximum and then decrease slowly with downstream distance increase. At the centerline, the temperature of counter-flow case is slightly higher than co-flow case, but the area of high temperature region for the co-flow case (left) is much bigger than the counter-flow case (right) displayed in figure 8(d). From the shapes of flame, we can tell the co-flow case (wider high temperature region) is much stable than the counter-flow case (narrow high temperature region). For the species profiles, figure 9 shows mean oxygen mole fraction contour for the cases of co-flow and counter-flow. We see that O_2 mole fraction falls below the value of 0.08 corresponding to the occurrence of the peak temperature. Also the peak temperature region may produce higher concentration of carbon dioxide. From figure 10, we can tell how plasma affects the production of CO_2 .

For the last problem of nanosecond pulsed plasma actuation, we compare our result with the baseline case shown in figure 11. Due to the combination effect of energy and momentum transfer from the nanosecond pulsed plasma actuators, we can see that the flame temperature is increased compared to the baseline case. The peak temperature is due to the local heating of the time-averaged power deposition from the nanosecond pulsed plasma actuators near

the walls. This heating may stabilize the combustion flame close the side walls. Figure 12 and 13 show the concentration distribution of reactants (O_2 and CH_4) and products (CO_2 and H_2O). For the contour of oxidizer and fuel, the concentration distribution is quite similar to the baseline case which means there is no significant momentum transfer to affect the size of IRZ and ORZ. However, the product of CO_2 is slightly increased near the side walls shown in figure 13. This increase is because the deposited energy enhances the chemical reaction for combustion.

V. Conclusion

The plasma governing equations as well as Navier-Stokes equations were solved with our in-house MIG flow code and commercial software ANSYS Fluent. Numerical results for the benchmark case are compared well with experimental data from Weigand *et al.* For the cases of co-flow and counter-flow using serpentine plasma actuators, our results demonstrate that plasma actuators can significantly influence the combustion process by changing the size of IRZ/ORZ enhancing the mixing of the surrounding fuel with air. The co-flow serpentine actuator creates larger IRZ than the baseline (no plasma) case predicting better flame stabilization. For the case of nanosecond pulsed plasma actuator, we can see slightly increase in temperature near the side walls of the combustion chamber. This increase may help the enhancement of chemical reaction for stabilizing the flame. Due to the lack of momentum from the state of art of rf powered plasma actuators, nanosecond pulsed actuators may benefit the design of plasma assisted gas turbine combustors. Our future study is to employ large eddy simulation for plasma assisted combustion using nanosecond pulsed actuators. This will help us to understand combustion instabilities during such instantaneous field.

Acknowledgments

The first author was partially supported by Yuan Ze University and the National Science Council, Taiwan, R.O.C under Grant No. NSC 101-2218-E-155-001.

References

- [1] U.S. Energy Information Agency, "Annual Energy Review 2011," DOE/EIA-0384(2011), Sep. 2012. (<http://www.eia.gov/totalenergy/data/annual/index.cfm>).
- [2] Moreau, E., "Airflow control by non-thermal plasma actuators," *J. Phys. D: Appl. Phys.*, Vol. 40, 2007, pp. 605-636.
- [3] Corke, T. C., Enloe, C. L., and Wilkinson, S. P., "Dielectric Barrier Discharge Plasma Actuators for Flow Control," *Annu. Rev. Fluid Mech.*, Vol. 42, 2010, pp. 505-529.
- [4] Gaintonde, D. V., Visbal, M. R. and Roy, S., "Three-dimensional plasma-based stall control simulations with coupled first-principles approached," ASME Joint US – European Engineering Summer Meeting, FEDSM2006-98553, 2006.
- [5] Visbal, M. R. and Gaintonde, D. V., "Control of vortical flows using plasma actuators," 44th AIAA Aerospace Sciences Meeting and Exhibit, AIAA-2006-505, 2006.
- [6] Wang, C. -C. and Roy, S., "Energy and force prediction for a nanosecond pulsed dielectric barrier discharge actuator," *J. Appl. Phys.*, Vol. 111, 2012, pp. 103302.
- [7] Starikovskii, A. Y., Nikipelov, A. A., Nudnova, M. M., and Roupassov, D. V., "SDBD plasma actuator with nanosecond pulse-periodic discharge," *Plasma Sources Sci. Technol.*, Vol. 18, 2009, pp. 034015.
- [8] Starikovskiy, A., and Aleksandrov, N., "Plasma-assisted ignition and combustion," *Prog. Energy Combust. Sci.*, Vol. 39, 2013, pp. 61-110.
- [9] Stage, S., Kim, Y., Ferreri, V., Rosocha, L. A., and Coates, D. M., "Flame images indicating combustion enhancement by dielectric barrier discharges," *IEEE Trans. Plasma Sci.*, Vol. 33, No. 2, 2005, pp. 316-317.
- [10] Leonov, S. B., and Yarantsev D. A., "Plasma-induced ignition and plasma-assisted combustion in high-speed flow," *Plasma Sources Sci. Technol.*, Vol. 16, 2007, pp. 132-138.
- [11] Starikovskaya, S. M., "Plasma assisted ignition and combustion," *J. Phys. D: Appl. Phys.*, Vol. 39, 2006, pp. R265–R299.
- [12] Roy, S. and Wang, C. -C., "Bulk fluid modification with horseshoe and serpentine plasma actuator," *J. Phys. D: Appl. Phys.*, Vol. 42, 2009, pp. 032004.
- [13] Wang, C. -C. and Roy, S., "Combustion stabilization using serpentine plasma actuators", *Appl. Phys. Lett.*, Vol. 99, 2011, 041502.
- [14] Roy, S., "Flow actuation using radio frequency in partially ionized collisional plasmas," *Appl. Phys. Lett.*, Vol. 86, 2005, 101502.
- [15] Kumar, H. and Roy, S., "Multidimensional hydrodynamic plasma-wall model for collisional plasma discharges with and without magnetic field effects," *Phys. Plasmas*, Vol. 12, No. 9, 2005, 093508.

[16] Singh, K. P., and Roy, S., "Modeling plasma actuators with air chemistry for effective flow control," *J. Appl. Phys.*, Vol. 101, No. 12, 2007, 123308.

[17] Hagelaar, G. J. M. and Pitchford, L. C., "Solving the Boltzmann equation to obtain electron transport coefficients and rate coefficients for fluid models," *Plasma Sources Sci. Technol.*, Vol. 14, 2005, pp. 722-733.

[18] Ellis, H. W., Pai, R. Y., McDaniel, E. W., Mason, E. A. and Viehland, L. A., "Transport properties of gaseous ions over a wide energy range," *At. Data Nucl. Data Tables*, Vol. 17, 1976, pp. 177-210.

[19] Kossyi, I. A., Kostinsky, A. Y., Matveyev, A. A. and Silakov, V. P., "Kinetic scheme of the non-equilibrium discharge in nitrogen-oxygen mixtures," *Plasma Sources Sci. Technol.*, Vol. 1, 1992, pp. 207-220.

[20] Poinsot, T., and Veynante, D., "Theoretical and numerical combustion," *R.T. Edwards Inc.*, 2nd edition, 2005, pp. 140-147.

[21] Flitti, A., and Pancheshnyi, S., "Gas heating in fast pulsed discharges in N_2O_2 mixtures," *Eur. Phys. J. Appl. Phys.*, Vol. 45, 2009, pp. 21001.

[22] Weigand, P., Meier, W., Duan1, X. R., Stricker, W., Aigner, M., "Investigations of swirl flames in a gas turbine model combustor: I. Flow field, structures, temperature, and species distributions," *Combust. Flame*, Vol. 144, 2006, pp. 205-224.

[23] Wang, C. -C., Durscher, R. J., and Roy, S., "Three-dimensional effects of curved plasma actuators in quiescent air," *J. Appl. Phys.*, Vol. 109, 2011, pp. 083305.

[24] Zito, J., Durscher, R., Soni, J., Roy, S., and Arnold, D., "Flow and Force Inducement Using Micro Size Dielectric Barrier Discharge Actuators," *Appl. Phys. Lett.*, Vol. 100, 2012, pp. 193502.

[25] Widenhorn, A., Noll, B., and Aigner, M., "Numerical characterization of a gas turbine model combustor," *High Performance Computing in Science and Engineering'09*, 2010, 179-195.

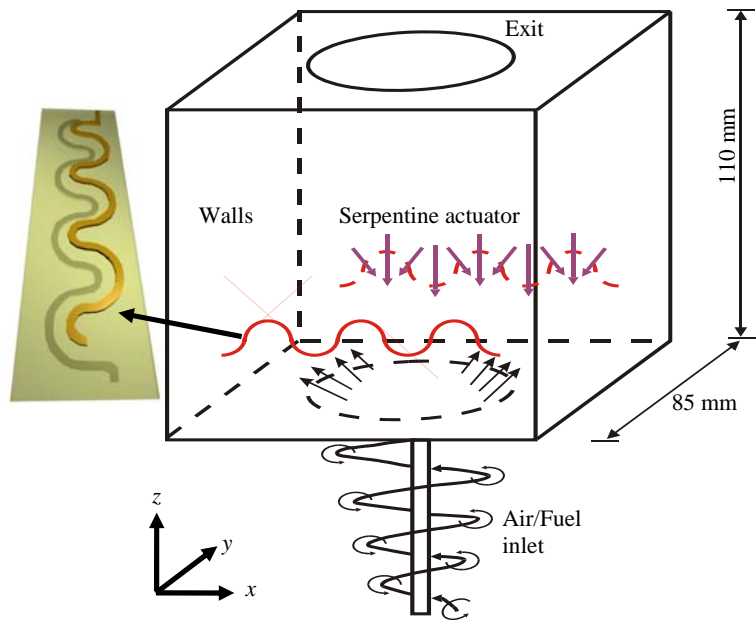


Figure 1. Schematic of a gas turbine combustor with serpentine actuators.

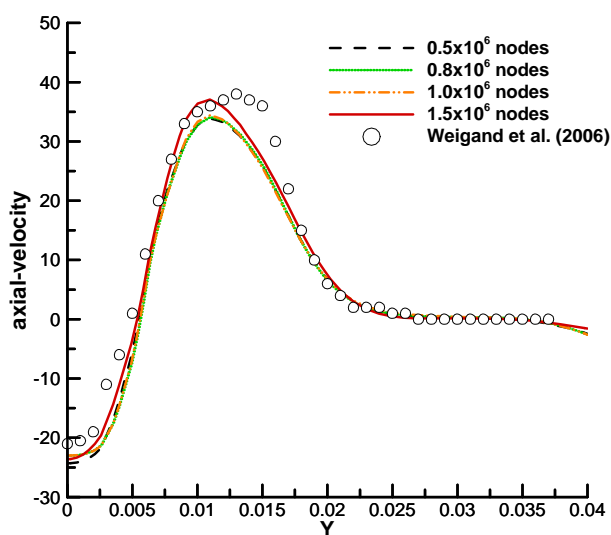


Figure 2. Grid independence.

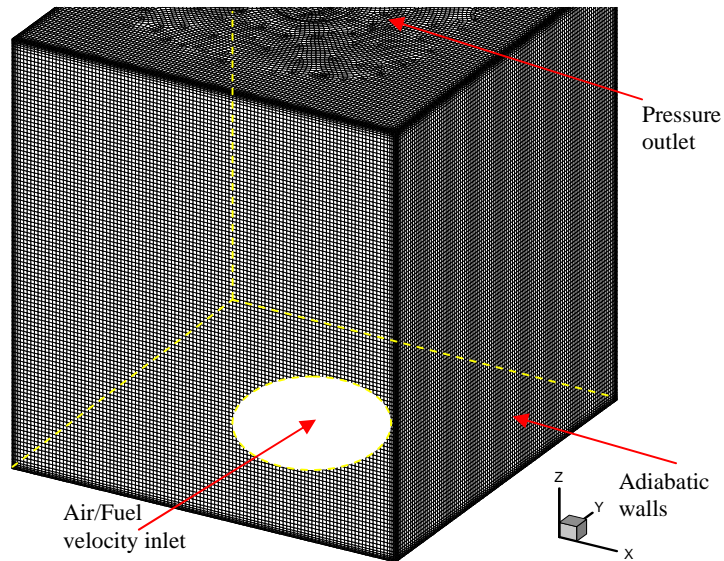


Figure 3. Computational grid of a gas turbine combustor and numerical boundary conditions.

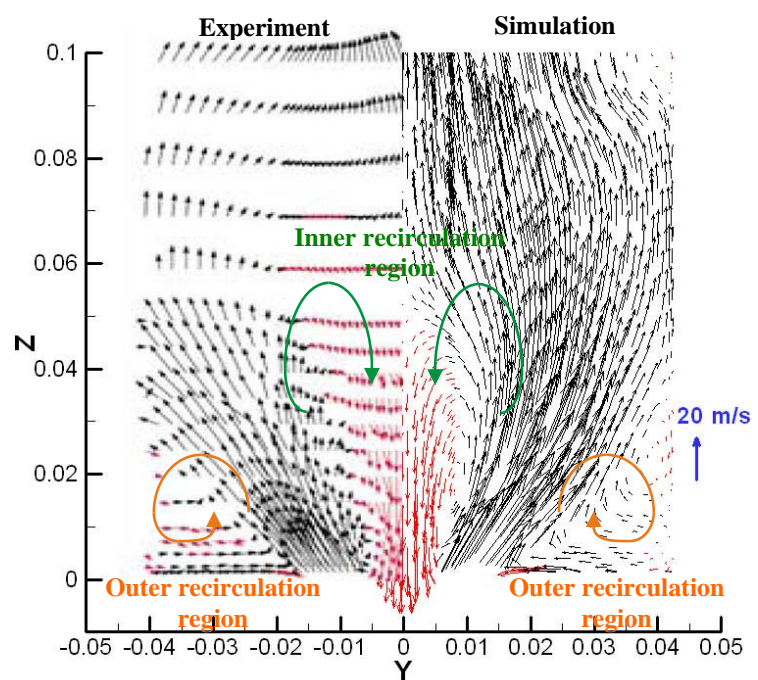


Figure 4. Comparison of experiment (left side) and simulation (right side) for time-averaged velocity vectors colored by axial velocity; negative axial velocities are displayed in red.

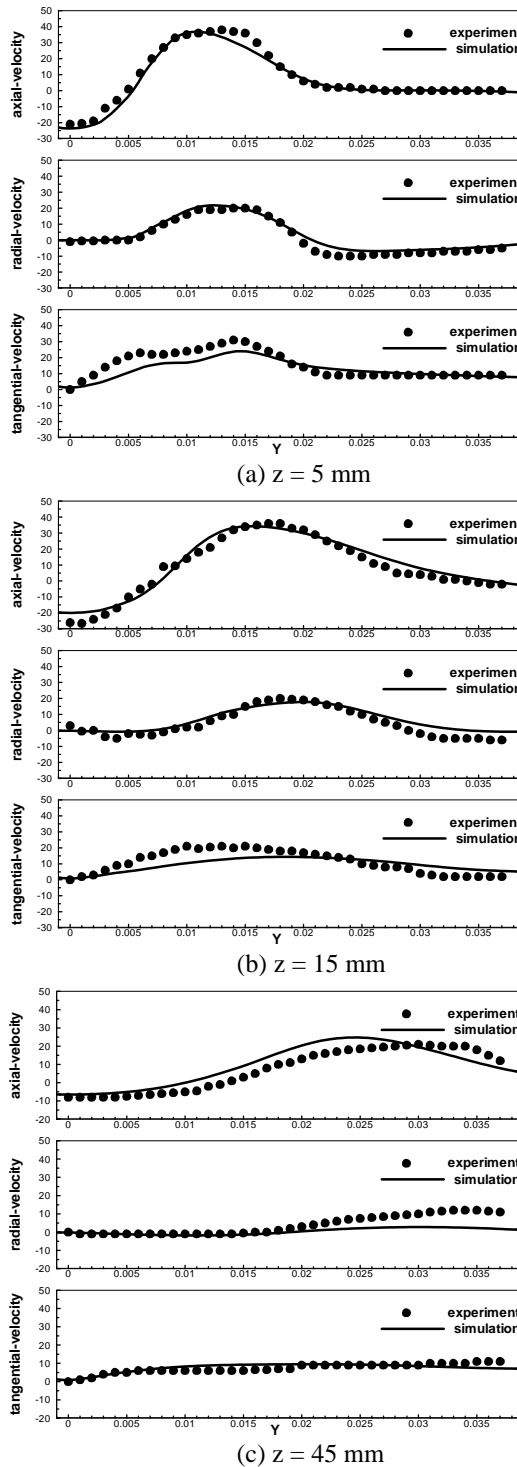


Figure 5. Time-averaged axial, radial and tangential velocity distributions along y -direction at (a) $z = 5$ mm, (b) $z = 15$ mm and (c) $z = 45$ mm; black circles (experiment), solid lines (simulation).

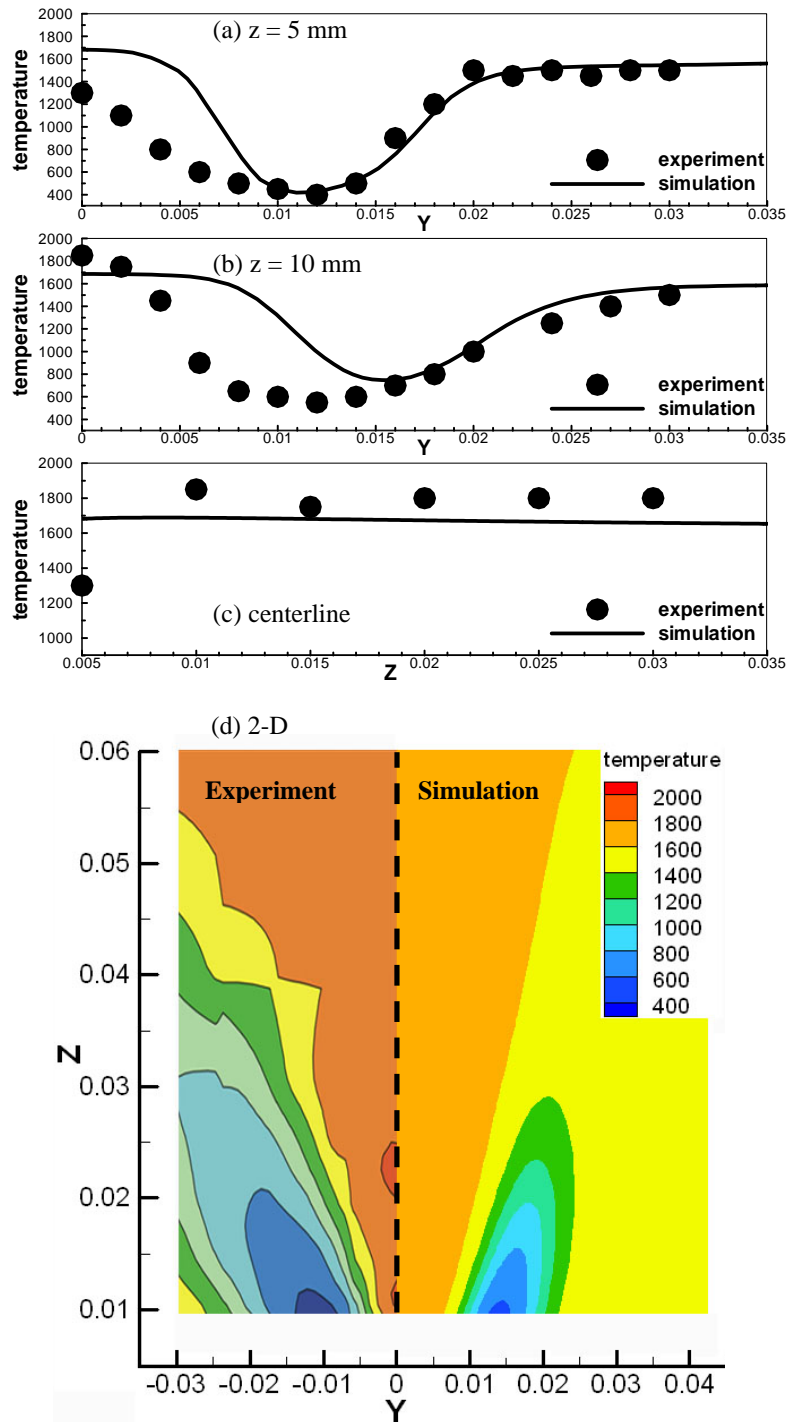


Figure 6. Comparison of experiment and simulation for time-averaged temperature at (a) $z = 5$ mm, (b) $z = 10$ mm, (c) centerline, and (d) two-dimensional contour; black circles (experiment), solid lines (simulation).

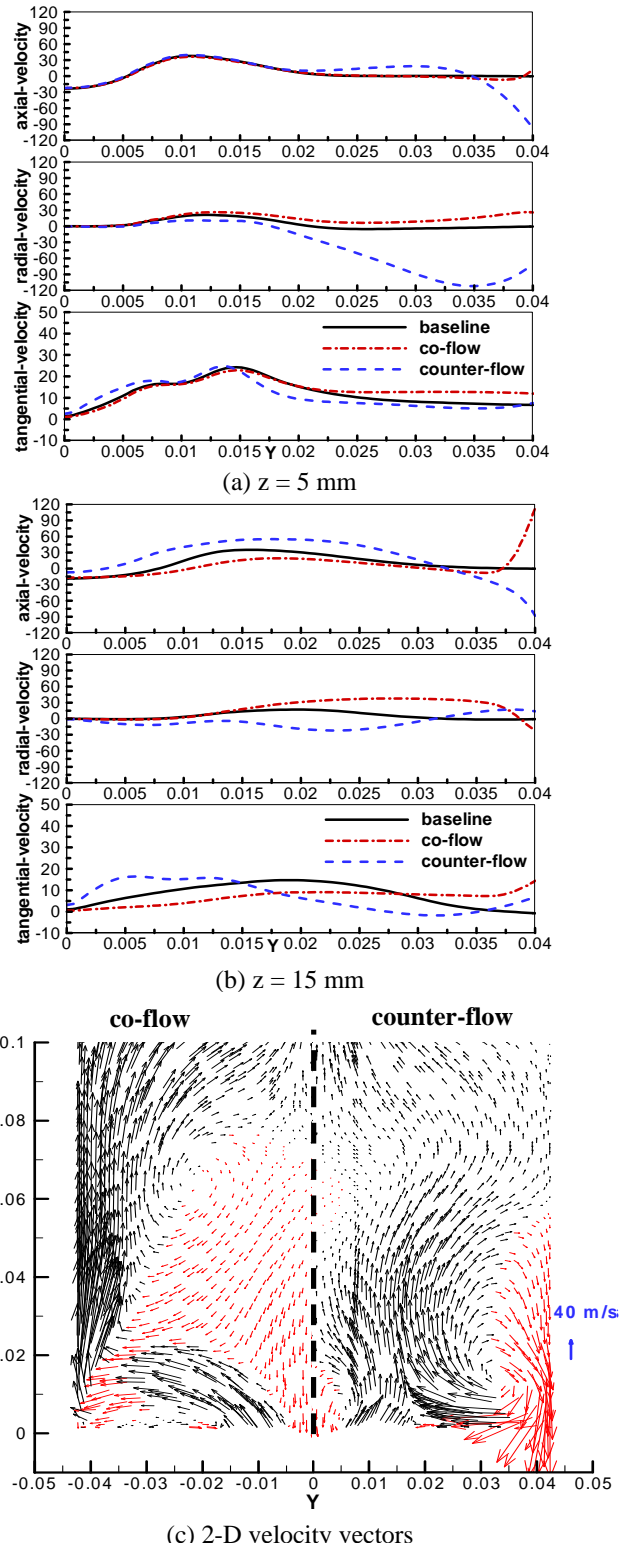


Figure 7. Time-averaged axial, radial and tangential velocity distributions with / without serpentine plasma actuation at the locations of (a) $z = 5 \text{ mm}$, (b) $z = 15 \text{ mm}$ and (c) two-dimensional velocity vectors; negative axial velocities are displayed in red.

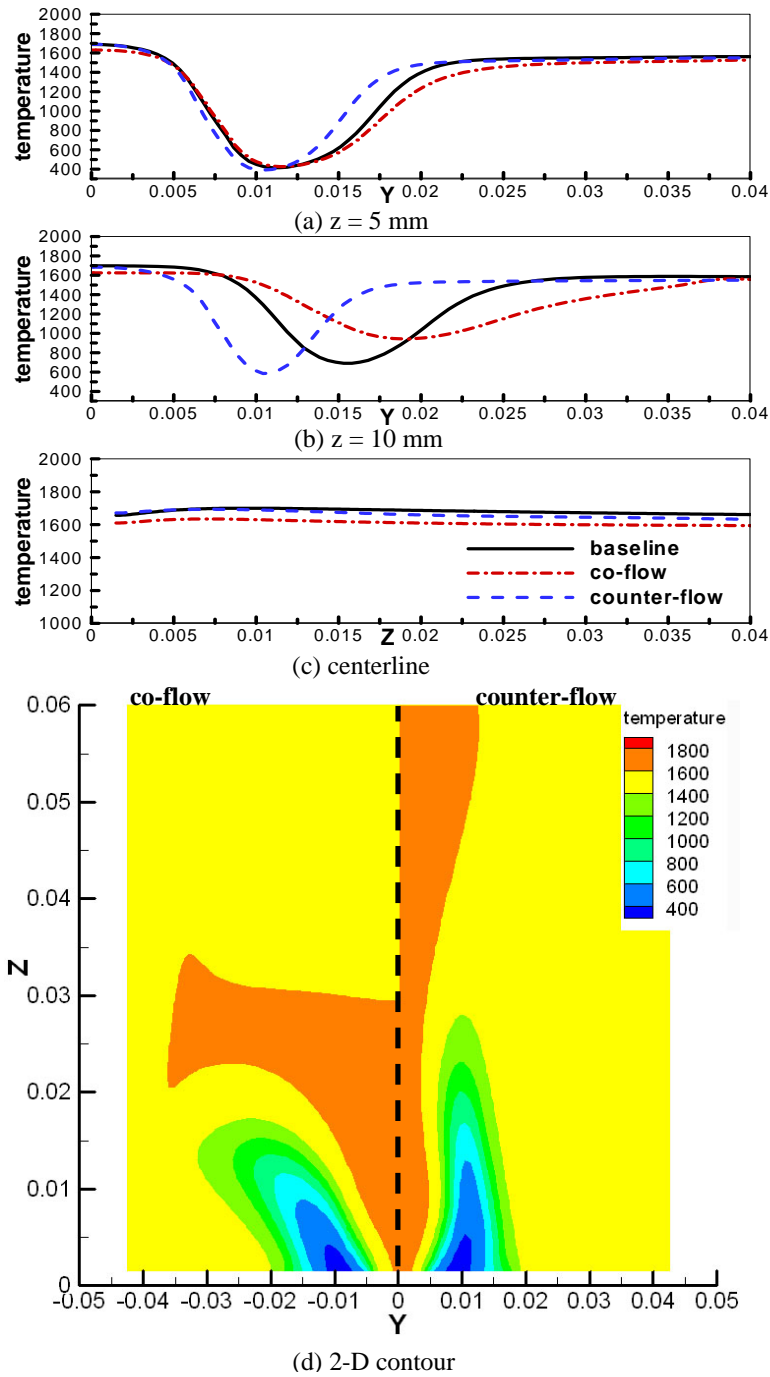


Figure 8. Time-averaged temperature distribution with / without serpentine plasma actuation at locations of (a) $z = 5 \text{ mm}$, (b) $z = 10 \text{ mm}$, (c) centerline, and (d) two-dimensional contour plot.

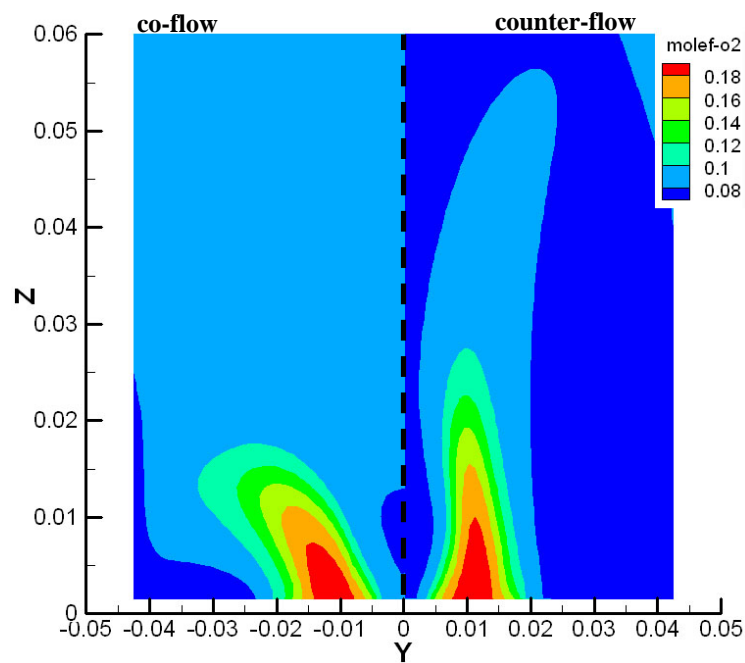


Figure 9. Mean oxygen mole fraction contour plot of co-flow (left side) and counter-flow (right side) with serpentine plasma actuation.

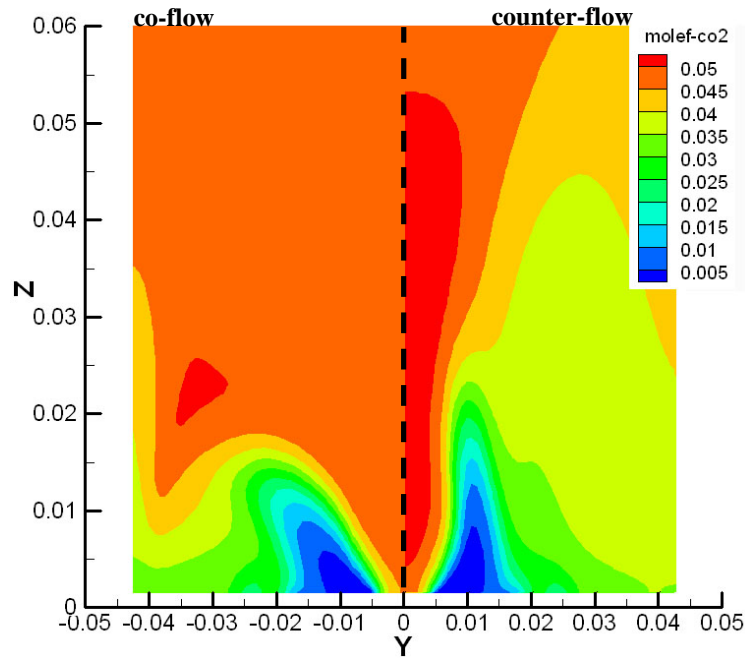


Figure 10. Mean carbon dioxide mole fraction contour plot of co-flow (left side) and counter-flow (right side) with serpentine plasma actuation.

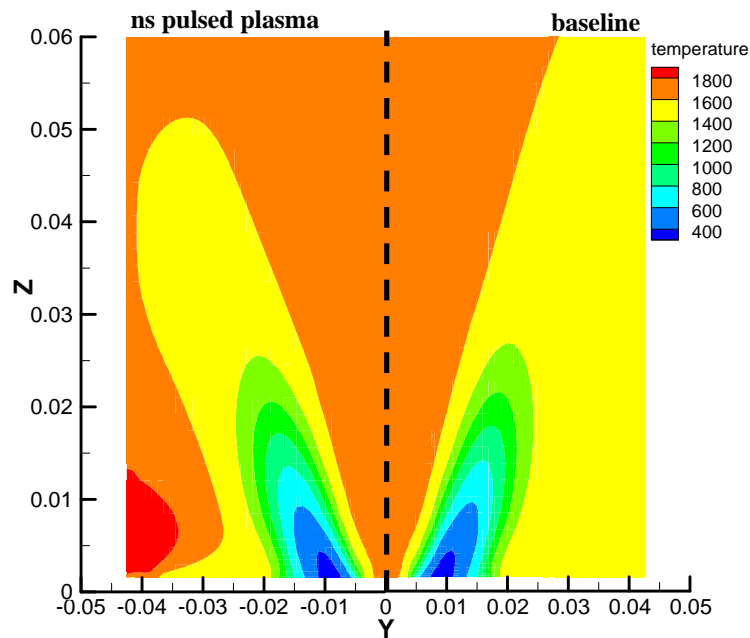


Figure 11. Time-averaged temperature contour with / without nanosecond pulsed plasma actuation.

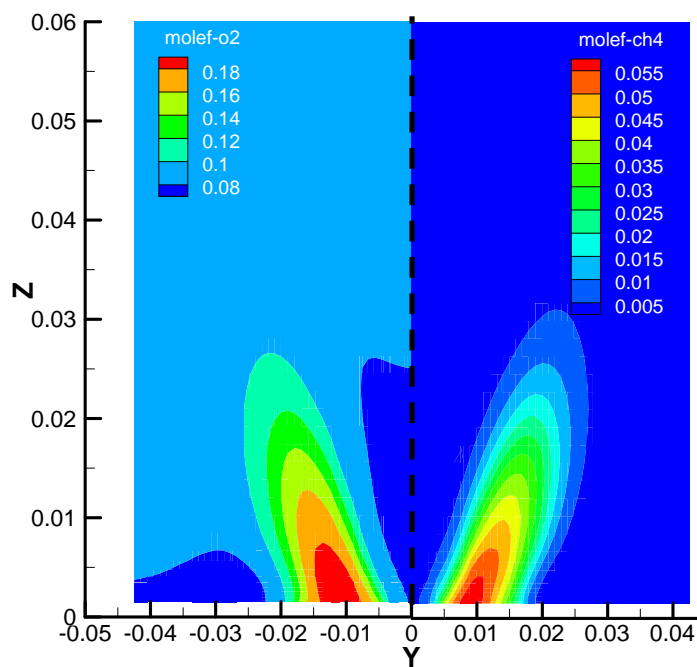


Figure 12. Mean oxygen (left side) and methane (right side) mole fraction contour plot with nanosecond pulsed plasma actuation.

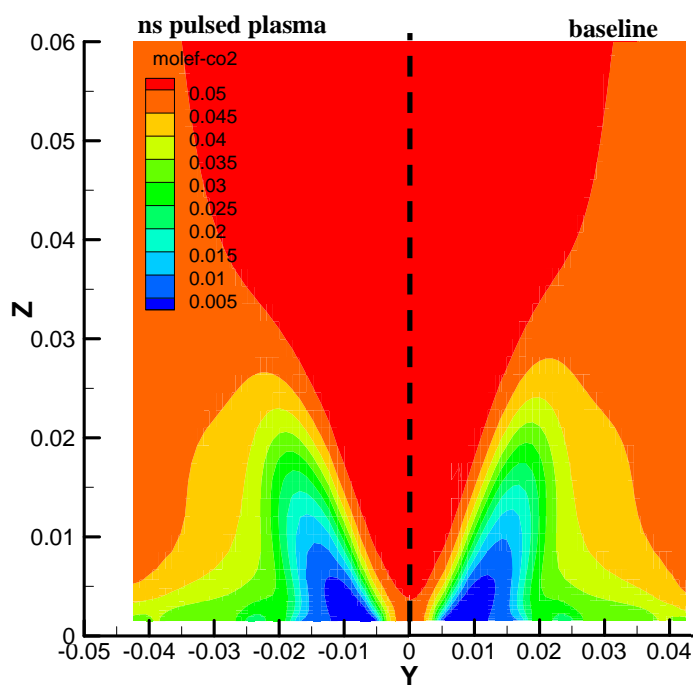


Figure 13. Mean carbon dioxide contour plot with / without nanosecond pulsed plasma actuation.